ADVANCED FUNCTIONAL MATERIALS
www.afm-journal.de

Plasmonic Nanoneedle Arrays with Enhanced Hot Electron Photodetection for Near-IR Imaging

Cheng Zhang, Binglin Huang, Haoyu Li, Hui Chen, Tong Yu, Bingchang Zhang,* Shaojun Wang, Changxu Liu, Yu Luo, Stefan A. Maier, and Xiaofeng Li**

Hot electron photodetection based on metallic nanostructures is attracting significant attention due to its potential to overcome the limitation of the traditional semiconductor bandgap. To enable efficient hot electron photodetection for practical applications, it is necessary to achieve broadband and perfect light absorption within extremely thin plasmonic nanostructures using cost-effective fabrication techniques. In this study, an ultrahigh optical absorption (up to 97.3% in average across the spectral range of 1200—2400 nm) is demonstrated in the ultrathin plasmonic nanoneedle arrays (NNs) with thickness of 10 nm, based on an all-wet metal-assisted chemical etching process. The efficient hot electron generation, transport, and injection at the nanoscale apex of the nanoneedles facilitate the photodetector to achieve a record low noise equivalent power (NEP) of 4.4×10^{-12} W Hz$^{-0.5}$ at the wavelength of 1300 nm. The hot-electron generation and injection process are elucidated through a transport model based on a Monte Carlo approach, which quantitatively matches the experimental data. The photodetector is further integrated into a light imaging system, as a demonstration of the exceptional imaging capabilities at the near-IR regime. The study presents a lithography-free, scalable, and cost-effective approach to enhance hot electron photodetection, with promising prospects for future imaging systems.

1. Introduction

Near-infrared (NIR) photodetectors are crucial in various technological applications, such as optical communication, imaging, sensing, etc.[1–4] Silicon-based photodetectors possess several advantages, including high stability, compatibility with complementary metal–oxide–semiconductor (CMOS) technology, and low cost.[5] Despite the benefits, they have a limitation of working in the telecommunication band due to transparency in this regime.[6] To address this limitation, alternative semiconductors with narrower bandgaps, such as germanium (Ge) and III–V [gallium antimonide (GaSb), indium arsenide (InAs), and gallium arsenide (GaAs)] and II–VI [mercury cadmium telluride (HgCdTe)] materials, have been developed for the NIR regime.[7–10] However, these materials are expensive, complex to process, and incompatible with silicon-based CMOS technology. One potential solution to this challenge is to harvest hot electrons generated from plasmon decay in metallic nanostructures.[11,12] However, plasmonic nanostructures with efficient hot electron photoconversion and ease of fabrication for practical photodetection technology remain elusive.[13–18]

In recent years, various metallic nanostructures have been explored to boost hot electron generation and extraction, including nanoantennas, gratings, embedded nanowires (NWs), nanoholes, nanobowls, pyramids, nanocubes, deep trenches, etc.[2,15–29] However, the broadband perfect absorption perfor-

C. Zhang, B. Huang, H. Li, H. Chen, T. Yu, B. Zhang, S. Wang, X. Li
School of Optoelectronic Science and Engineering & Collaborative Innovation Center of Suzhou Nano Science and Technology
Soochow University
Suzhou 215006, China
E-mail: zhangc@suda.edu.cn; zhangbingchang@suda.edu.cn; xfli@suda.edu.cn

C. Zhang, B. Huang, H. Li, H. Chen, T. Yu, B. Zhang, S. Wang, X. Li
Key Lab of Advanced Optical Manufacturing Technologies of Jiangsu Province
Key Lab of Modern Optical Technologies of Education Ministry of China
Soochow University
Suzhou 215006, China

C. Liu
Centre for Metamaterial Research & Innovation
Department of Engineering
University of Exeter
Exeter EX4 4QF, UK

Y. Luo
School of Electrical and Electronic Engineering
Nanyang Technological University
Nanyang Avenue, Singapore 639798, Singapore

S. A. Maier
School of Physics and Astronomy
Monash University
Clayton, Victoria 3800, Australia

S. A. Maier
The Blackett Laboratory
Department of Physics
Imperial College London
London SW7 2AZ, UK

The ORCID identification number(s) for the author(s) of this article can be found under https://doi.org/10.1002/adfm.202304368

DOI: 10.1002/adfm.202304368

mance is still limited, especially for gratings that only support one narrowband plasmon resonance. In addition, the thickness of plasmonic nanostructures is close to or greater than the electron diffusion length, which leads to severe thermalization loss during hot electron transport to the Schottky interface.[2,17–20] Meanwhile, most metallic nanostructures have delicately designed configurations that require complicated and expensive fabrication processes such as lithography and dry-etching. Although the metal-assisted chemical etching (MACE) method offers a cost-effective alternative, the reported works still require sophisticated and costly equipment to form metal catalysts, such as high-vacuum coating systems and rapid thermal processing.[5,18,21] Furthermore, the obtained morphology is limited to nanoholes since only silicon under the metal catalysts is etched, which results in insufficient broadband perfect absorption performance and a discontinuous film coating on vertical sidewalls. More importantly, there is a trade-off between maximizing near-field enhancement and minimizing the reflection on the nanostructure, which may limit the generation of energetic carriers. On one hand, strong near-field enhancement at the surface of plasmonic nanostructures is desired for the efficient production of hot electrons.[30] On the other hand, the strong light–matter interaction may induce intense scattering and consequently increase the reflection, reducing total efficiency of metallic nanostructures. To fully explore the potential and practical applications of hot electron photodetection, it is imperative to achieve giant near-field enhancement and broadband perfect absorption within extremely thin plasmonic nanostructures. Achieving a hot electron photodetection system with all desired features mentioned above remains as an open question.

In this study, we provide a solution to the challenge, proposing and experimentally realizing an efficient broadband hot electron photodetector covering telecommunication bands, based on high aspect-ratio plasmonic Au/Si nanoneedle arrays (NNs) fabricated using an all-wet MACE process to further eliminate the need for costly and complex equipment in catalyst formation. The proposed plasmonic NNs can achieve the giant near-field enhancement and broadband absorption simultaneously, owing to the tapered morphology formed naturally by the all-wet MACE process. The hybrid plasmonic mode along the tapered needle offers giant field enhancement and broadband response,[31–34] while the tapered geometry varying along the light propagation direction induces an effective graded refractive index, dramatically reducing the reflection of the structured substrate.[35] As a result, we achieve an average absorption of 97.3% over the spectral range of 1200−2400 nm in the plasmonic nanoneedles with thickness of 10 nm, much smaller than the electron diffusion length. The efficient hot electron generation, transport, and injection at the nanoscale apex of the plasmonic nanoneedles contribute to a record low noise equivalent power (NEP) of 4.4×10^{-12} W Hz$^{-0.5}$ at the wavelength of 1300 nm. The Monte Carlo simulation shows that the corresponding responsivity exceeds the limit that can be achieved under a planar configuration with a film thickness of only 5 nm. By reducing the Schottky barrier to the typical value of 0.5 eV for Ti/n-Si contacts, the responsivity could be improved to a record-high value of 15 mA W^{-1}. Furthermore, we integrate the photodetector into a light imaging system, and demonstrate its imaging capabilities under near-IR light illumination below the Si bandgap. Our study presents a lithography-free, scalable, and cost-effective approach to enhance hot electron photodetection with promising prospects for future imaging systems.

2. Results and Discussion

2.1. Design Principles of Plasmonic Nanoneedles

Figure 1a illustrates the schematic diagram of the plasmonic core-shell nanoneedles, which consist of Si nanoneedles coated with a conformal 10 nm Au film on the surface. D_1 (D_2) and H represent the top (bottom) cross-sectional diameter and height of the nanoneedles, respectively. When light is incident on the plasmonic nanoneedles, it first excites the localized surface plasmon resonances at the apex, leading to a strongly enhanced electric field intensity; the propagating surface plasmon resonances can then be excited and propagate along the gold/air interface, while the penetrating light insides the Si nanoneedles can form waveguide resonances arising from total internal reflection at the Au/Si interface.[36,37] To demonstrate this principle, plasmonic nanoneedles with $D_1 = 50$ nm, $D_2 = 300$ nm, and $H = 5$ μm were designed as an example. Figure 1b–d shows the normalized electric field intensity in the xz cross-sectional plane at $\lambda = 1300$ nm, divided into three parts for clarity. All localized surface plasmon resonances, propagating surface plasmon resonances, and waveguide resonances can be identified clearly. The local electric field at the bottom plasmonic NNs is increased by more than 3 orders of magnitude. The typical absorption distributions at different xy cross-sectional planes at $\lambda = 1300$ nm and $\lambda = 1800$ nm are illustrated in Figure 1e,f, respectively. At the bottom of the plasmonic nanoneedles, the propagating surface plasmon resonances and waveguide resonances are coupled to form a hybrid mode, as displayed in Figure 1f.[36] Due to the varying cross-sectional dimensions in the plasmonic nanoneedles, various optical modes in different wavelengths and orders can be supported. Thus, under the appropriate design of plasmonic nanoneedles, broadband, and significant optical absorption can be achieved. Figure 1g shows the optical performance of the exampled plasmonics nanoneedles. Due to the gradual change of the effective refractive index in plasmonic nanoneedles, the optical reflection loss is negligible across the broad spectral band.[38] An average absorption of 85% is realized in the plasmonic nanoneedles with an ultrathin Au film of only 10 nm, which indicates a good light trapping capability.

The optical performance of plasmonic nanoneedles is strongly dependent on the geometric parameters. For all calculations, the geometric parameters were fixed as $D_1 = 50$ nm, $D_2 = 300$ nm, and $H = 5$ μm unless otherwise specified. Figure 1h shows the average absorption as a function of height and bottom cross-sectional diameter, revealing that the high aspect-ratio (H/D_2) nanoneedles with small vertex angles are more efficient for light absorption. Figure 1i shows that increasing the height improves the average absorption due to more excited optical absorption modes in plasmonic nanoneedles (see Figure S1a, Supporting Information). However, for a large bottom cross-sectional diameter, only specific high-order narrowband optical modes are supported (see Figure S1b, Supporting Information), resulting in a limited average absorption as shown in Figure 1j. In particular, for the high aspect-ratio plasmonic nanoneedles with $D_2 < 180$ nm, the optical absorption is beyond 95% across

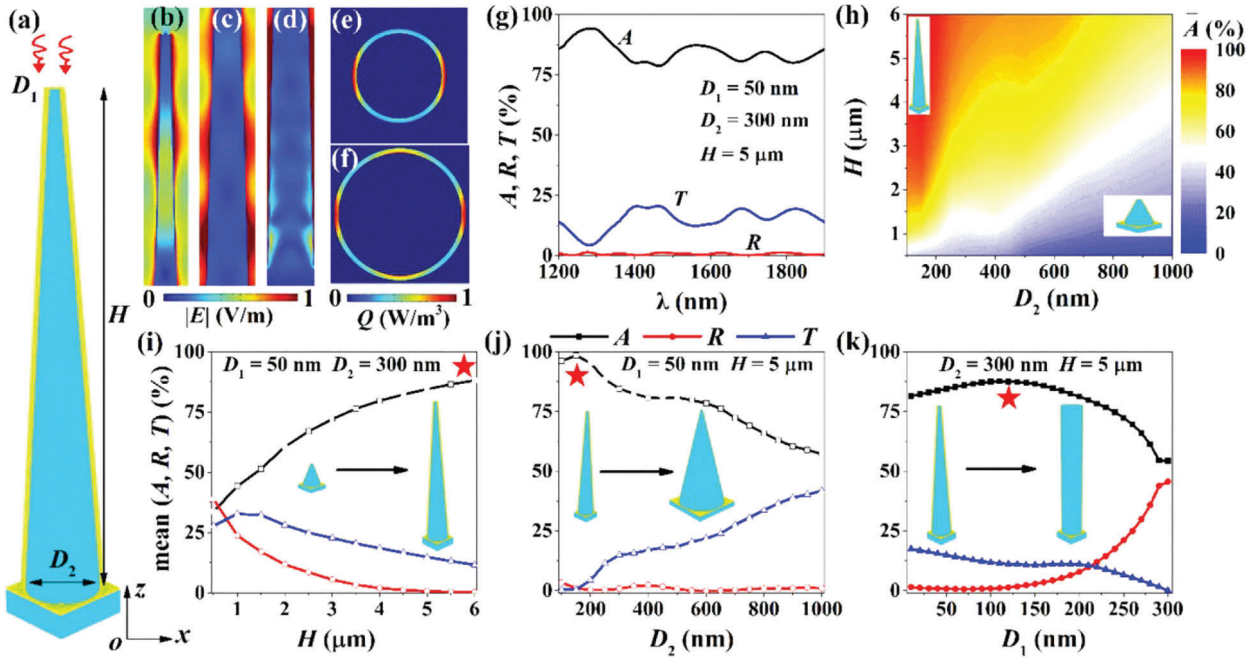

Figure 1. a) Schematic diagram of Si-core/Au-shell plasmonic nanoneedles, where D_1, D_2, and H represent the core diameters of the top, bottom cross-sectional areas and height, respectively. Examples of typical normalized electric field b–d) at λ = 1300 nm) and absorption mode profiles at e) λ = 1300 nm, h = 2 μm; f) λ = 1800 nm, h = 0.3 μm, where h is the vertical distance from the bottom to the cut plane of nanoneedles. g) Optical performance of plasmonic nanoneedles with D_1 = 50 nm, D_2 = 300 nm, and H = 5 μm. h) Average absorption of plasmonic nanoneedles versus height and bottom diameter. i-k) Dependence of the average absorption, reflection and transmission of plasmonic nanoneedles on height, bottom diameter, and top diameter, respectively, with D_1 = 50 nm, D_2 = 300 nm, and H = 5 μm unless otherwise specified.

the entire spectral band (see Figure S1b, Supporting Information). Figure 1k shows that a slight increase in the top cross-sectional diameter enhances the optical mode resonances, leading to an improved average absorption (Figure S1c, Supporting Information). However, a large top cross-sectional diameter leads to limited optical modes and decreased absorption, as in the case of the nanowire structure (NWs, $D_1 = D_2$).[36] Therefore, plasmonic nanoneedles with a high aspect ratio and small vertex angle may be ideal building blocks for efficient hot electron devices.

2.2. Fabrication and Optical Performance of Plasmonic Nanoneedles

Based on the predicted excellent performance, plasmonic core-shell nanoneedles were prepared by carefully controlling the catalyst evolution from deposition to etching stages in an all-wet MACE process.[39] **Figure 2**a–c shows a schematic diagram of the fabrication procedure. First, a silicon wafer was soaked in a seed solution consisting of 0.02 M $AgNO_3$ and 4.8 M HF for a designated reaction time, forming Ag nanoparticles as catalysts for the subsequent MACE process. The wafer was then transferred to an etching solution composed of 4.8 M HF and 0.4 M H_2O_2 for 15 min and immersed in HNO_3 solution to remove the Ag catalysts. Finally, metal films of Au (10 nm) and Al (100 nm) were deposited to form plasmonic nanoneedles and Ohmic contact on the backside, respectively. Here, a relatively long reaction time of 60 s was used to form large Ag particles that are closely interconnected, which not only acted as catalysts but also participated in the etching process. As the size of the Ag particles decreased during the etching process, the diameters of the etched silicon nanostructures gradually increased, resulting in the formation of Si nanoneedles. For comparison, a reaction time of 20 s was used to form small Ag particles, as used in the conventional MACE process (Figure S2a–c, Supporting Information). In this way, only the silicon beneath the Ag particles was etched and formed disordered Si NWs.

The vertically standing Si nanoneedles with apexes are clearly seen in Figure 2d–f. They have a height of ≈2.5 μm, an average bottom cross-sectional diameter of ≈200 nm, and a vertex angle close to 8°. The inclined surface of Si nanoneedles allows for nearly uniform deposition of the thin Au film, as shown in Figure 2h–j. As a comparison, silicon nanowires and those coated with a thin Au film are shown in Figure S3 (Supporting Information) in the supporting information. Figure 2g shows that the reflectivity of Si NNs is slightly lower than that of NWs due to the gradual change in the effective refractive index, as shown in the inset.[36,40] Figure 2k illustrates that the reflectivity is further reduced, and the average absorption reaches 97.3% in photodetectors based on plasmonic Au/Si NNs. To better explain the reflectivity and absorption measured, we conducted a statistical analysis on H and D_2 of 25 Si nanoneedles, as depicted in Figure S4 (Supporting Information) in the supporting information. The average height and diameter of the measured Si nanoneedles are ≈3 μm and 350 nm, respectively; these plasmonic nanoneedles with varying H and D_2 exhibit a similar optical absorption of ≈70% (Figure S5, Supporting Information). It is noted that

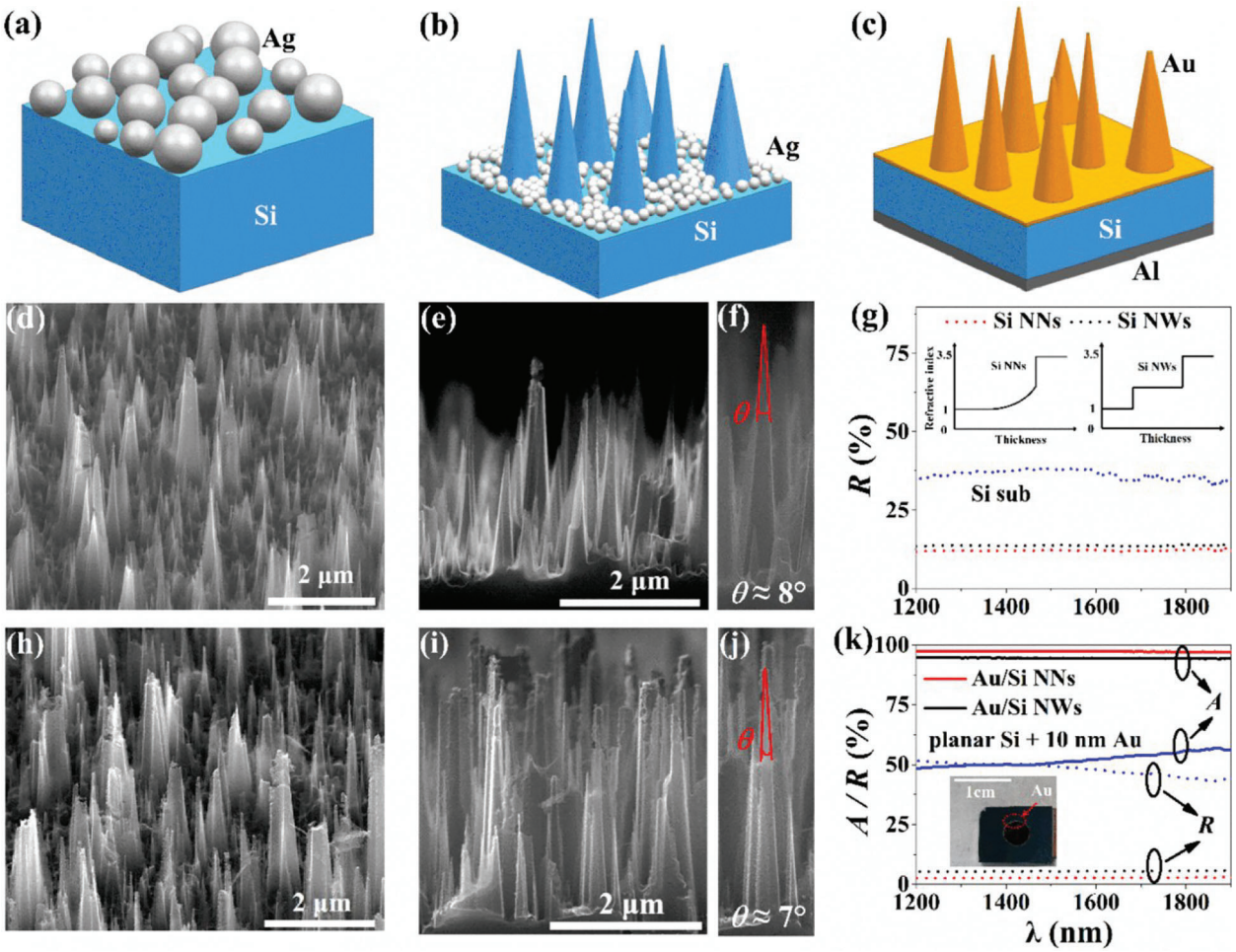

Figure 2. a–c) Fabrication procedure for the plasmonic nanoneedles-based hot electron photodetector (NNs-HE PD). d–f) and h–j) are scanning electron microscopy (SEM) images of plasmonic nanoneedles before and after Au film deposition, respectively. The vertex angles are measured and indicated. g) Reflection of Si NNs, NWs, and planar substrate. k) Reflection and absorption of the hot-electron photodetector based on Au/Si NNs, NWs, and planar structures. The profiles of the effective index of Si NNs/NWs and the optical image of the photodetector are inserted in (g) and (k), respectively.

the absorption is further improved in the photodetector due to the utilization of a backside contact of Al film. The average optical reflection in these plasmonic nanoneedles is relatively close to the measured average reflection, considering the measurement error (Figure S6, Supporting Information). The inset of Figure 2k shows that for front-side contacting, a 100 nm Au thin film was deposited on a specific region of the plasmonic NNs, as indicated by the red circle. With the excellent optical performance and simple fabrication process that is free of lithography or dry-etching processes using masks, Au/Si NNs are expected to have an outstanding electrical response for practical hot electron applications.

2.3. Electrical Response of Plasmonic Nanoneedles-Based Hot-Electron Photodetector

To study the quality of the Schottky junction formed in the plasmonic Au/Si nanoneedles, the current–voltage (I–V) characteristic was measured under dark conditions at room temperature. **Figure 3**a exhibits a clear rectifying behavior in the I–V characteristic with a dark current (I_d) of 0.4 nA at zero-bias, indicating excellent contact of the thin film Au on the surface of Si nanoneedles. The experimental data agree well with the theoretical fitting curve based on the thermionic emission model (Figure S7, Supporting Information).[41,42] The extracted Schottky barrier height is 0.758 eV, which is consistent with that of the typical Au/Si contact.[2] Figure 3b presents the obvious on-off switching under light illumination of different wavelengths. The measured responsivity (*Res.*) of the plasmonic NNs-HE PD is 2–3 times (2–3 orders of magnitude) higher than that based on Au/Si NWs (nanoantennas), as shown in Figure 3c. Although the barrier height is high, the responsivity of the plasmonic NNs-HE PD still reaches 2.56 mA W^{-1} at λ = 1300 nm, which is higher than that of reported devices based on gratings, embedded nanowires, disordered nanoholes, nanobowls, and micropyramids.[18–23,26] The prominent improvement of photocurrents from plasmonic NWs to NNs at all three wavelengths unambiguously verifies the enhanced hot electron generation and injection in plasmonic NNs, as the photocurrent

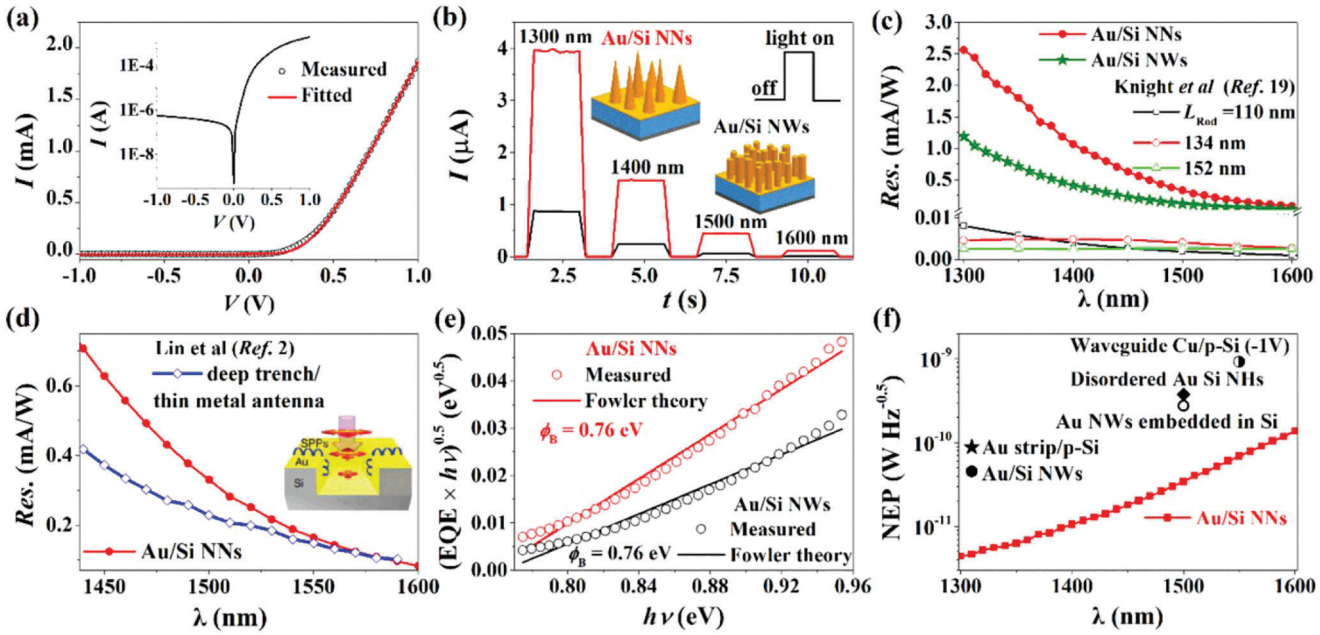

Figure 3. a) Measured and fitted current-voltage (*I*–*V*) curves of the plasmonic NNs-HE PD under dark conditions based on thermal emission theory. b) Measured current under light illumination of various wavelengths. c,d) Measured responsivity of the plasmonic NNs-HE PD with that based on nanorods and deep trench/thin metal antennas, respectively. e) Fowler fitting to the measured EQE spectrum. f) NEP spectrum of the plasmonic NNs-HE PD. The typical NEPs in the hot electron photodetector based on various structures are inserted for comparison.

boost is far beyond the absorption improvement shown in Figure 2k.

Under identical light illumination conditions provided by a tunable laser (i.e., high-power illumination), the responsivity of the plasmonic NNs-HE PD is even 1.7 times higher than that based on deep-trench/thin-metal active antennas (at $\lambda = 1440$ nm), as shown in Figure 3d. From the Fowler model by plotting $\sqrt{EQE \times h\nu}$ *vs* $h\nu$ (EQE is the external quantum efficiency, h is the Planck constant, and ν is the light frequency) in Figure 3e, the extracted Schottky barrier was found to be 0.76 eV, which agrees well with that estimated from the dark *I*–*V* measurement based on thermionic emission theory.[43] Based on the measured responsivity and dark current, the NEP ($\frac{\sqrt{2eI_d}}{Res}$, e is the electron charge) that describes the minimal detectable optical power at a given electrical bandwidth (1 Hz) was obtained.[29] Figure 3f shows that the plasmonic NNs-HE PD can detect optical signals in the pW regime, which is lower than that based on nanowires, strips, embedded nanowires, nanoholes, and waveguides.[21,26,44–46] The enhanced electrical performance further suggests that such a plasmonic nanoneedles structure might be a good candidate for hot electron photodetection.

2.4. Hot Electron Transport in Plasmonic NNs-HE PD

In order to better understand the hot electron physical behavior from generation, transport to injection processes, and find strategies to further promote device performance, we developed an electron transport model based on a Monte Carlo approach.[47] The model accounts for resistive loss, initial hot electron energy distribution upon excitation, electron-electron, and electron-phonon scattering events. It is noted that for the plasmonic NNs-HE PD proposed here, the metal film thickness is ever smaller than the mean free path of electrons. The electron transport model based on the phenomenological models is failed.[47] As schematically shown in **Figure 4**a, hot electrons are generated by an event of photon absorption. However, part of the absorbed photon energy (i.e., resistive loss) is dissipated thermally without generating hot electrons.[48] The efficiency of plasmon decay into hot electrons (η_{eh}) ranges from 60% to 90% depending on the size and shape of the metallic nanostructures.[48] The initial hot electron energy distribution is described by the electron density of states and the Fermi distribution function:[49,50]

$$D\ (E) = \frac{\rho\,(E - h\upsilon) f\,(E - h\upsilon)\,\rho\,(E)\left[1 - f\,(E)\right]}{\int \rho\,(E - h\upsilon) f\,(E - h\upsilon)\,\rho\,(E)\left[1 - f\,(E)\right] dE} \quad (1)$$

where E is the energy of the excited electron, $h\upsilon$ is the photon energy, $\rho(E–h\upsilon)$ [$\rho(E)$] is the parabolic electron density of states at the initial [final] energy level, and $f(E–h\upsilon)$ [$f(E)$] is the corresponding Fermi distribution function. Figure 4b shows the calculated hot electron energy distributions under light excitation of different wavelengths. Considering the barrier height of 0.76 eV measured in the proposed devices, only a small fraction of electrons can be collected. During transport, hot electrons can undergo electron-electron scatterings with cold electrons, resulting in the loss of excess energy. In addition, hot electrons can undergo electron-phonon scatterings, which modify the propagation directions isotopically with maintained energy.[47] The energy-dependent hot electron mean free path due to the electron-electron and electron-phonon scatterings are taken from Ref. [47] and [48]. Due to the complexity of the plasmonic

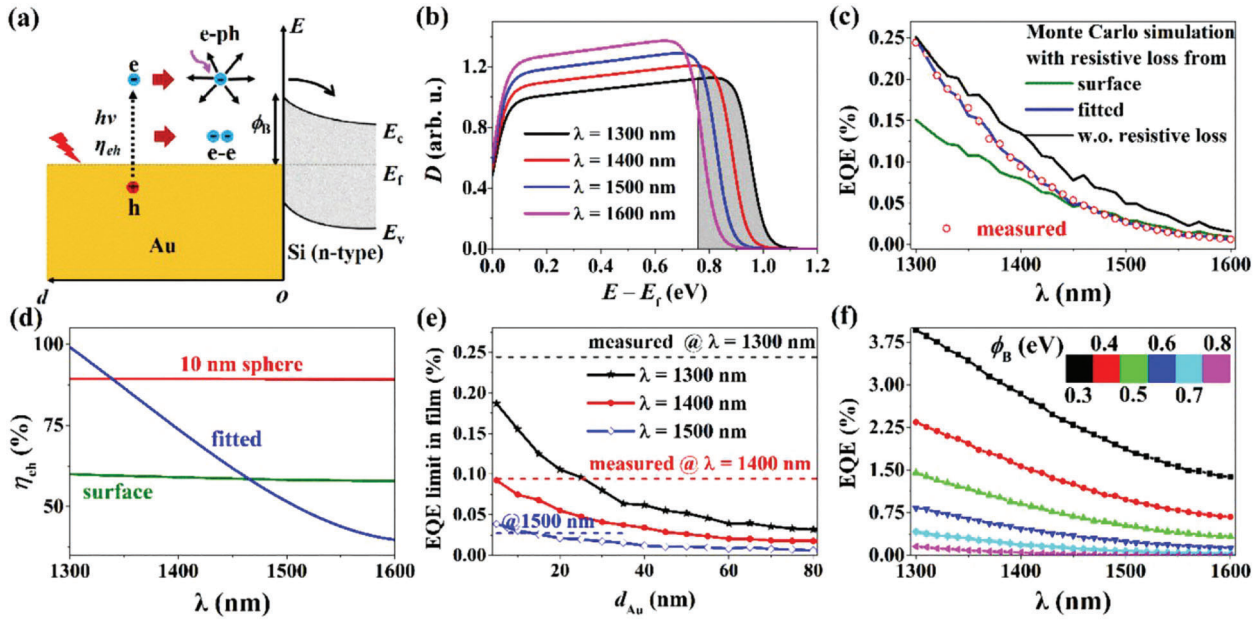

Figure 4. a) Schematic diagram of hot electron generation, transport, and injection processes. b) Initial hot electron energy distribution upon excitation under various wavelengths. The shaded region represents energy beyond the Schottky barrier height. c) Calculated and measured EQE spectra based on the developed electron transport model from a Monte Carlo method. d) Fitted efficiency spectrum of plasmons decay into hot electrons in plasmonic NNs-HE PD, with that from 10 nm spheres and semi-infinite surface inserted. e) Limit of EQE in a planar hot electron device at three typical wavelengths as a function of metal film thickness. The measured EQEs at different wavelengths in the plasmonic NNs-HE PD with a constant Au film thickness of 10 nm are inserted. f) Predicted EQE spectra of the plasmonic NNs-HE PD with various Schottky barrier heights.

NNs-HE PD, we considered a simplified configuration of a 10 nm thin Au film on a semiconductor with a uniform hot-electron generation and a large number of electrons (≈1 000 000) to understand the fundamentals of the hot electron transport process.

Figure 4c presents the EQE spectra obtained from the measurement and Monte Carlo simulations. By using η_{eh} as a fitting parameter, the measured and simulated EQE spectra are consistent, which demonstrates the effectiveness of the electron transport model. Neglecting resistive loss would result in overestimated hot electron generation efficiency and higher EQE compared to experimental results. However, using resistive loss from the semi-infinite surface would lead to underestimated hot electron generation efficiency and a lower EQE. Figure 4d shows the fitted efficiency of plasmon decay into hot electrons as a function of wavelength. It is found that the fitted η_{eh} at short wavelengths is higher compared to that in 10 nm diameter spheres. It is noted that in Monte Carlo simulations, we did not take account of the locally enhanced electric field and relaxation of electron momentum mismatch in plasmonic nanoneedles, which are known to promote the hot electron generation and collection. Thus, the higher fitted η_{eh}, relative to that in 10-diameter spheres, can be attributed to the effect of these two factors. However, at longer wavelengths, since more hot electrons are generated at the gold/air interface, away from the Schottky junction, the fitted η_{eh} is lower than that from the semi-infinite surface.

In order to demonstrate the role of the nanoneedles in improving the hot electron photodetection performance, we compared the measured EQEs of the plasmonic NNs-HE PD with the limit of that in a planar geometry. Here, based on the developed electron transport model, we calculated the EQE limit of hot electrons in the planar geometry assuming perfect optical absorption.[47] Figure 4e illustrates the EQE limits of planar hot electron devices as a function of Au film thickness at three typical wavelengths, along with the corresponding measured values in the plasmonic NNs-HE PD with a constant Au film thickness of 10 nm. It is surprising that at $\lambda = 1300$ nm, the EQE of the plasmonic NNs-HE PD is even 1.3 times greater than that of the planar device with an Au film thickness of only 5 nm. The measured EQEs in the plasmonic NNs-HE PD are close to or higher than the efficiency limit in the planar device with the same film thickness.

Although the EQE of the plasmonic NNs-HE PD already exceeds that based on many other types of structures, and even surpasses the theoretical limit of planar devices, it remains to be explored whether other strategies can be employed to further enhance EQE and to what extent it can be improved. Considering that the Schottky barrier height is interface-dependent and can even be reduced to 0.3 eV when using p-type silicon,[51] Figure 4f illustrates the EQE spectra of the plasmonic NNs-HE PD with different barrier heights. By decreasing the Schottky barrier to 0.5 eV for typical Ti/n-Si contacts, the responsivity reaches a record high of 15 mA/W at $\lambda = 1300$ nm. It is expected that the EQE in the plasmonic NNs-HE PD with a p-type Si substrate could be significantly improved to 4%, up to ≈16 times compared to the current case using n-type Si. However, the low barrier height can increase the dark current, requiring a tradeoff to be considered.

2.5. NIR Imaging with Plasmonic NNs-HE PD

The NIR imaging capability of the plasmonic NNs-HE PD at telecommunication wavelengths was evaluated further in

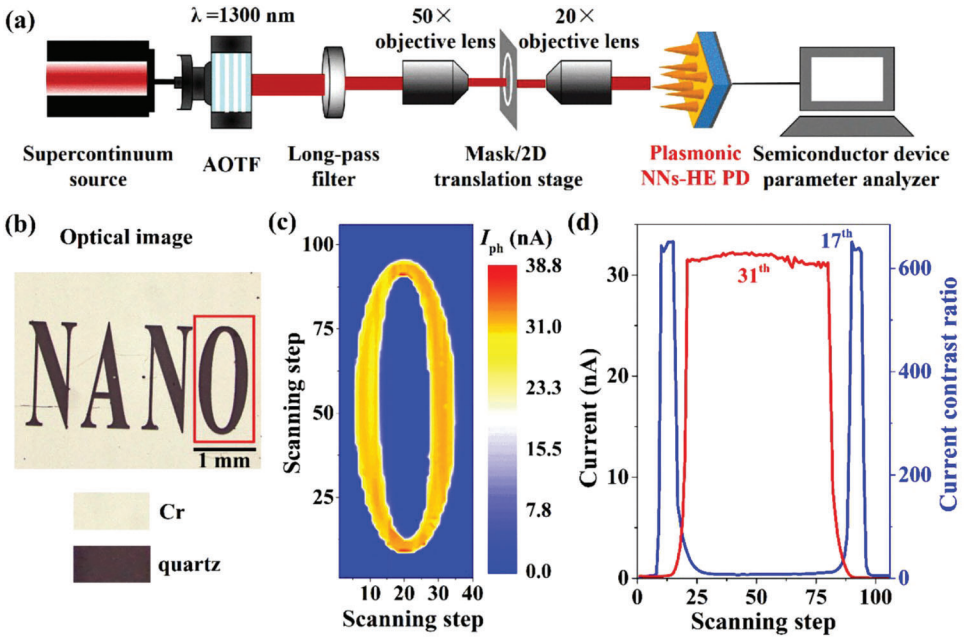

Figure 5. a) Schematic diagram of the NIR imaging measurement system. AOTF is the acousto-optical tunable filter. b) Optical image of the mask: Cr/quartz structure. The boxed region indicates the imaged area in (c). c) Image obtained by the plasmonic NNs-HE PD. d) Measured line scanning current along the 17th and 31th steps in the horizontal direction.

Figure 5a. The plasmonic NNs-HE PD records the position-dependent photocurrent when scanning the mask. Figure 5b shows an optical image of the photolithography mask with the letters "Nano". The mask consists of an optically thick layer of chromium (Cr) on a quartz substrate, with most of the regions being opaque due to the deposition of Cr. However, the letter portion is transparent, allowing light to transmit and generate a photocurrent in the photodetector. Figure 5c illustrates the photocurrent image of the letter "o" when illuminated at $\lambda = 1300$ nm, well below the bandgap of Si. The plasmonic NNs-HE PD produced a detectable and reliable photocurrent. The line-scanning current in Figure 5d shows that the current contrast ratio (i.e., the ratio of photocurrent to dark current) can reach 600, which further demonstrates the good capability of the plasmonic NNs-HE PD for NIR imaging at telecommunication wavelengths.

Finally, we compare the fabrication challenge/cost and performance of previously reported hot electron photodetectors with plasmonic NNs-HE PD (**Table 1**). The reported hot electron devices have a responsivity ranging from 0.008 to 3 mA/W at $\lambda = 1300$ nm. Most of the devices were fabricated using electron beam lithography (EBL), ultra-violet lithography, vacuum film deposition, and annealing to prepare Si nanostructures with high/medium fabrication challenge/cost. In contrast, the nanoneedles structure can be obtained using a simple, scalable, and low-challenge/cost method of an all-wet MACE process. Besides, the responsivity of the plasmonic NNs-HE PD is higher than that of most reported devices featuring plasmonic nanostructures, including nanorods, gratings, nanowires, nanotrenches, nanoholes, nanopillars, and nanobowls, etc, although the Schottky barrier of our device is higher.[2,15,17,19,20,22,23,26,52] The performance can be further improved under backside illumination. Due to the low dark current and enhanced responsivity, the NEP of the plasmonic NNs-HE PD is among the lowest yet reported. In addition, the plasmonic nanoneedles exhibit broadband and significant absorption, even at large incidence angles up to 60° ≈ 70° for both TE- and TM-polarized incidences (Figure S8, Supporting Information). Thus, our device has the best application potential among reported hot electron photodetectors considering ultralow noise, high responsivity, and low-cost fabrication, which will pave the way for practical applications.

3. Conclusion

In summary, we have demonstrated an efficient hot electron photodetector based on high aspect-ratio plasmonic nanoneedles. The multiple optical modes, including localized surface plasmons, propagating surface plasmons, and waveguide mode contribute to an average optical absorption of 97.3% over the entire NIR spectral range in the plasmonic nanoneedles with a thickness of 10 nm. The enhanced hot electron generation, transport, and injection at the nanoscale apex of the plasmonic nanoneedles contribute to the lowest reported noise equivalent power of 4.4×10^{-12} W Hz$^{-0.5}$ at the wavelength of 1300 nm. The developed electron transport model based on a Monte Carlo approach depicts the physical behavior of hot electrons from generation to injection processes and the predicted efficiency is consistent with the experiment. The measured efficiency is greater than the limit that can be achieved under a planar configuration with a film thickness of 5 nm. Finally, the plasmonic NNs-HE PD exhibits a superior high-resolution imaging capability with a high current contrast ratio.

Table 1. Comparison of the fabrication challenge/cost and performance of typical hot electron photodetectors.

Device structure	Fabrication method	Fabrication challenge/cost	Barrier height [eV]	Responsivity [mA W^{-1}]		Dark current	NEP [W/$\sqrt{\text{Hz}}$]	Reference
				λ = 1300 nm	1500 nm			
Au nanoantennas/Si	EBL	High	0.5	0.008	0.004	NA	NA	[19]
Au grating/Si	EBL	High	0.5	0.58	0.47	NA	NA	[20]
Metamaterial Au/Si	EBL	High	0.54	3	1.8	NA	NA	[15]
Au nanowires embedded in Si	EBL	High	0.52	NA	0.065	1×10^{-9} A	$2.75^{a)} \times 10^{-10}$	[26]
Deep-trench/thin Au/Si antenna	I-line lithography	Medium	0.75	$3^{b)}$	$0.5^{b)}$	NA	NA	[2]
				NA	0.23			
Disordered Au/Si nanoholes	Sputtering, RTP, wet-etching	Medium	0.66	1.1	0.16	1×10^{-6} A	1.6×10^{-9}	[21]
Au film on Si nanopillar	Vacuum deposition, annealing	Medium	0.81	0.43	NA	4×10^{-8} A	2.6×10^{-10}	[46]
Au film on Si nanobowl	Thermal evaporation, RTP, wet-etching	Medium	0.47	0.34	0.29	2.5×10^{-7} A	8.3×10^{-10}	[22]
Au film on Si micropyramid	Wet-etching	Low	$0.74^{c)}$	0.5	0.1	5×10^{-10} A	2.5×10^{-11}	[23]
Disordered Au/Si nanoneedles	Wet-etching	Low	0.76	2.56	0.33	4×10^{-10} A	4.4×10^{-12}	This work

The device performance is measured under no electrical bias. NEP is calculated at λ = 1300 nm unless otherwise specified. RTP: rapid thermal process. [a] calculated at λ = 1500 nm; [b] calculated under low-intensity light using a tungsten lamp with a monochromator; [c] calculated from responsivity spectrum using Fowler fitting method.

4. Experimental Section

Device Fabrication and Characterization: All devices were fabricated using n-type silicon wafers with a resistivity of 1–10 Ω cm, which were coated on both sides with a 500 nm thermal oxide layer. To begin the process, the front side of the wafer was protected using tape with a 5 mm diameter punched hole. The exposed oxide on both sides was then etched away by immersing the wafer in an HF solution. Next, the silicon wafer was soaked in a seed solution consisting of 0.02 M $AgNO_3$ and 4.8 M HF for a designated reaction time. The silicon wafer was then transferred to an etching solution composed of 4.8 M HF and 0.4 M H_2O_2 for 15 min. Finally, the silicon wafer was immersed in HNO_3 solution to remove the Ag catalysts, after which two layers of Au (10 nm) and Al (100 nm) were deposited on the front and back sides, respectively.

To fabricate Si nanowires, small Ag particles were formed using a reaction time of 20 s, resulting in etching of only the silicon beneath the particles. To fabricate Si nanoneedles, a longer reaction time of 60 s was used to form large Ag particles that were closely interconnected, acting not only as catalysts but also participating in the etching process. As the size of the Ag particles decreased during the etching process, the diameters of the etched silicon nanostructures gradually increased, leading to the formation of Si NNs. For front-side contacting, a thin Au film of 100 nm was deposited on a specific region of the plasmonic nanoneedles, as indicated by the red circle in the inset of Figure 2k. For backside contacting, a 100 nm Al film was deposited, that was in contact with a Cu metal piece via Ag paste. As a result, the active area of the photodetector was ≈15.7 mm^2, which corresponded to ≈80% of the area of the hole in the protective tape. The microscopic morphologies were characterized by scanning electron microscopes (ZEISS, Sigma 300; Hitachi, SU5000).

Optical and Electrical Measurements: For the optical measurement, all reflectance spectra were obtained using a Perkin–Elmer Lambda 1050S + UV/VIS/NIR spectrometer equipped with a 150 mm InGaAs integrating sphere. For the electrical measurement, the device was illuminated by a NKT Photonics supercontinuum laser with an acousto-optical tunable filter to select the wavelength. The laser beam was focused by an objective (Mitutoyo, 10×, 0.26 NA). The photocurrent was recorded with a Keysight B1500A semiconductor device parameter analyzer. The optical power was measured by an optical power meter from Thorlabs (S148C).

Supporting Information

Supporting Information is available from the Wiley Online Library or from the author.

Acknowledgements

This work was supported by the National Natural Science Foundation of China (62120106001, 62004134), the Suzhou Science and Technology Plan Projects (SYG202124), the Jiangsu Provincial Key Laboratory of Advanced Optical Manufacturing Technology (ZZ2112), the Natural Science Foundation of Jiangsu Province (BK20200857), the Natural Science Foundation of the Jiangsu Higher Education Institutions of China (20KJA510003), and the Priority Academic Program Development (PAPD) of Jiangsu Higher Education Institutions. S.A.M. additionaly acknowledges the EPSRC (EP/W017075/1) and the Lee-Lucas Chair in Physics. Y.L. acknowledges funding support from A*Star AME IRG Grant (A20E5c0095) and National Research Fundation Competitive Research Programe (NRF-CRP22-2019-0006)

Conflict of Interest

The authors declare no conflict of interest.

Data Availability Statement

The data that support the findings of this study are available from the corresponding author upon reasonable request.

Keywords

hot electrons, imaging, near-IR photodetection, plasmonic nanoneedles

Received: April 20, 2023
Revised: June 16, 2023
Published online:

[1] B. T. Giugni, A. Toma, M. Malerba, A. Alabastri, R. Proietti Zaccaria, M. I. Stockman, E. Di Fabrizio, *Nat. Nanotechnol.* **2013**, *8*, 845.
[2] K. T. Lin, H. L. Chen, Y. S. Lai, C. C. Yu, *Nat. Commun.* **2014**, *5*, 3288.
[3] L. Wen, L. Liang, X. Yang, Z. Liu, Q. Chen, *ACS Nano* **2019**, *13*, 6963.
[4] C. Zhang, Y. Luo, S. Maier, X. Li, *Laser Photonics Rev.* **2022**, *16*, 2100714.
[5] Y. Dong, J. Li, W. Liang, X. Nan, L. Wen, Q. Chen, *ACS Photonics* **2022**, *9*, 3705.
[6] W. Li, J. G. Valentine, *Nanophotonics* **2017**, *6*, 177.
[7] J. Michel, J. Liu, L. C. Kimerling, *Nat. Photonics* **2010**, *4*, 527.
[8] S. Wirths, R. Geiger, N. Von Den Driesch, G. Mussler, T. Stoica, S. Mantl, Z. Ikonic, M. Luysberg, S. Chiussi, J. M. Hartmann, H. Sigg, J. Faist, D. Buca, D. Grützmacher, *Nat. Photonics* **2015**, *9*, 88.
[9] B. Feng, J. Zhu, B. Lu, F. Liu, Y. Chen, *ACS Nano* **2019**, *13*, 8433.
[10] R. R. LaPierre, M. Robson, K. M. Azizur-Rahman, P. Kuyanov, *J. Phys. D. Appl. Phys.* **2017**, *50*, 123001.
[11] C. Clavero, *Nat. Photonics* **2014**, *8*, 95.
[12] M. Brongersma, N. J. Halas, P. Nordlander, *Nat. Nanotechnol.* **2015**, *10*, 25.
[13] C. Zhang, G. Cao, S. Wu, W. Shao, V. Giannini, S. A. Maier, X. Li, *Nano Energy* **2019**, *55*, 164.
[14] T. Matsui, Y. Li, M. H. M. Hsu, C. Merckling, R. F. Oulton, L. F. Cohen, S. A. Maier, *Adv. Funct. Mater.* **2018**, *28*, 1705829.
[15] W. Li, J. Valentine, *Nano Lett.* **2014**, *14*, 3510.
[16] C. Zhang, K. Wu, V. Giannini, X. Li, *ACS Nano* **2017**, *11*, 1719.
[17] C. Zhang, Q. Qian, L. Qin, X. Zhu, C. Wang, X. Li, *ACS Photonics* **2018**, *5*, 5079.
[18] L. Wen, Y. Chen, W. Liu, Q. Su, J. Grant, Z. Qi, Q. Wang, Q. Chen, *Laser Photon. Rev.* **2017**, *11*, 1700059.
[19] M. W. Knight, H. Sobhani, P. Nordlander, N. J. Halas, *Science* **2011**, *332*, 702.
[20] A. Sobhani, M. W. Knight, Y. Wang, B. Zheng, N. S. King, L. V. Browm, Z. Fang, P. Nordlander, N. J. Halas, *Nat. Commun.* **2013**, *4*, 1643.
[21] L. Wen, Y. Chen, L. Liang, Q. Chen, *ACS Photonics* **2018**, *5*, 581.
[22] L. Zhou, C. Zhang, L. Li, T. Liu, K. Li, S. Wu, X. Li, *Opt. Express* **2021**, *29*, 15505.
[23] Y. Zhai, Y. Li, J. Ji, Z. Wu, Q. Wang, *ACS Appl. Nano Mater.* **2020**, *3*, 149.
[24] B. Desiatov, I. Goykhman, N. Mazurski, J. Shappir, J. B. Khurgin, U. Levy, *Optica* **2015**, *2*, 335.
[25] C. Frydendahl, M. Grajower, J. Bar-David, R. Zektzer, N. Mazurski, J. Shappir, U. Levy, *Optica* **2020**, *7*, 371.
[26] M. W. Knight, Y. Wang, A. S. Urban, A. Sobhani, N. J. Halas, *Nano Lett.* **2013**, *13*, 1687.
[27] M. Tanzid, A. Ahmadivand, R. Zhang, B. Cerjan, A. Sobhani, S. Yazdi, P. Nordlander, N. J. Halas, *ACS Photonics* **2018**, *5*, 3472.
[28] Y. Zhu, H. Xu, P. Yu, Z. Wang, *Appl. Phys. Rev.* **2021**, *8*, 021305.
[29] M. Grajower, B. Desiatov, N. Mazurski, J. Shappir, J. B. Khurgin, U. Levy, *ACS Photonics* **2017**, *4*, 1015.
[30] G. V. Hartland, L. V. Besteiro, P. Johns, A. O. Govorov, *ACS Energy Lett.* **2017**, *2*, 1641.
[31] M. I. Stockman, *Phys. Rev. Lett.* **2004**, *93*, 137404.
[32] Y. Luo, D. Y. Lei, S. A. Maier, J. B. Pendry, *Phys. Rev. Lett.* **2012**, *108*, 023901.
[33] D. K. Gramotnev, S. I. Bozhevolnyi, *Nat. Photonics* **2014**, *8*, 13.
[34] P. Dombi, Z. Pápa, J. Vogelsang, S. V. Yalunin, M. Sivis, G. Herink, S. Schäfer, P. Groß, C. Ropers, C. Lienau, *Rev. Mod. Phys.* **2020**, *92*, 025003.
[35] Y. Huang, S. Chattopadhyay, Y. Jen, C. Peng, T. Liu, Y. Hsu, C. Pan, H. Lo, C. Hsu, Y. Chang, C. Lee, K. Chen, L. Chen, *Nat. Nanotechnol.* **2007**, *2*, 770.
[36] L. Zhou, X. Yu, J. Zhu, *Nano Lett.* **2014**, *14*, 1093.
[37] Q. Chen, K. Liu, Y. Zhou, X. Wang, K. Wu, H. Li, E. Pensa, J. Fu, M. Miyauchi, E. Cortés, M. Liu, *Nano Lett.* **2022**, *22*, 6276.
[38] J. Zhu, Z. Yu, G. F. Burkhard, C. M. Hsu, S. T. Connor, Y. Xu, Q. Wang, M. McGehee, S. Fan, Y. Cui, *Nano Lett.* **2009**, *9*, 279.
[39] C. Bian, B. Zhang, Z. Zhang, H. Chen, D. Zhang, S. Wang, Y. Jing, L. He, J. Jie, X. Zhang, *ACS Omega* **2022**, *7*, 2234.
[40] S. Sarkar, A. A. Elsayed, Y. M. Sabry, F. Marty, J. Drévillon, X. Liu, Z. Liang, E. Richalot, P. Basset, E. Nefzaoui, T. Bourouina, *Adv. Photonics Res.* **2022**, *4*, 2200223.
[41] S. K. Cheung, N. W. Cheung, *Appl. Phys. Lett.* **1986**, *49*, 85.
[42] N. A. Güsken, A. Lauri, Y. Li, T. Matsui, S. A. Maier, *ACS Photonics* **2019**, *6*, 953.
[43] C. Scales, P. Berini, *IEEE J. Quant. Electron.* **2010**, *46*, 633.
[44] Z. Yang, K. Du, H. Wang, F. Lu, Y. Pang, J. Wang, X. Gan, W. Zhang, T. Mei, S. J. Chua, *Nanotechnology* **2019**, *30*, 075204.
[45] A. Akbari, P. Berini, *Appl. Phys. Lett.* **2009**, *95*, 021104.
[46] M. Casalino, L. Sirleto, M. Iodice, N. Saffioti, M. Gioffre, I. Rendina, G. Coppola, *Appl. Phys. Lett.* **2010**, *96*, 241112.
[47] E. Blandre, D. Jalas, A. Y. Petrov, M. Eich, *ACS Photonics* **2018**, *5*, 3613.
[48] A. M. Brown, R. Sundararaman, P. Narang, W. A. Goddard III, H. A. Atwater, *ACS Nano* **2016**, *10*, 957.
[49] T. Gong, J. N. Munday, *Opt. Mater. Express* **2015**, *5*, 2501.
[50] T. P. White, K. R. Catchpole, *Appl. Phys. Lett.* **2012**, *101*, 073905.
[51] M. Alavirad, A. Olivieri, L. Roy, P. Berini, *Opt. Express* **2016**, *24*, 22544.
[52] Y. Ajiki, T. Kan, M. Yahiro, A. Hamada, J. Adachi, C. Adachi, K. Matsumoto, I. Shimoyama, *Appl. Phys. Lett.* **2016**, *108*, 151102.

ADVANCED FUNCTIONAL MATERIALS

Supporting Information

for *Adv. Funct. Mater.*, DOI 10.1002/adfm.202304368

Plasmonic Nanoneedle Arrays with Enhanced Hot Electron Photodetection for Near-IR Imaging

Cheng Zhang, Binglin Huang, Haoyu Li, Hui Chen, Tong Yu, Bingchang Zhang*, Shaojun Wang, Changxu Liu, Yu Luo, Stefan A. Maier and Xiaofeng Li**

Supporting Information

Plasmonic Nanoneedle Arrays with Enhanced Hot Electron Photodetection for Near-IR Imaging

Cheng Zhang, Binglin Huang, Haoyu Li, Hui Chen, Tong Yu, Bingchang Zhang,* Shaojun Wang, Changxu Liu, Yu Luo, Stefan A. Maier, and Xiaofeng Li**

Supporting figures

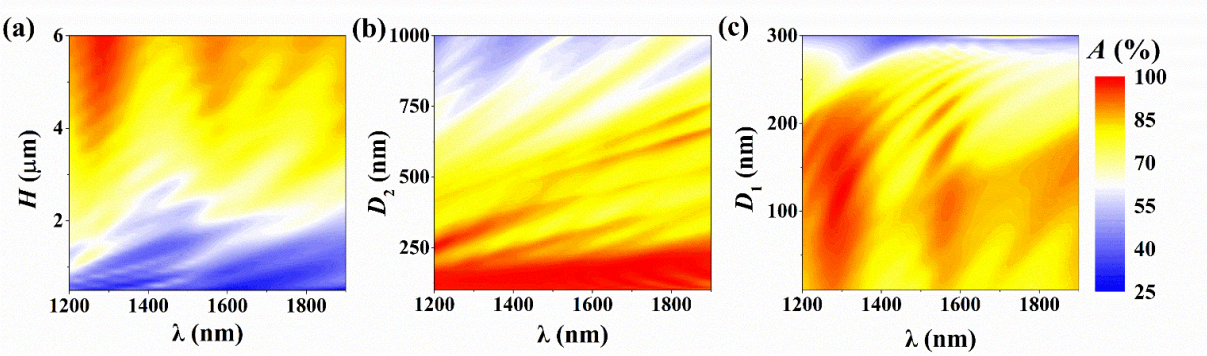

Figure S1. Absorption as a function of wavelength and height (a), bottom diameter (b), and top diameter (c) in plasmonic Au/Si nanoneedles with D_1 = 50 nm, D_2 = 300 nm, and H = 5 μm (unless otherwise specified).

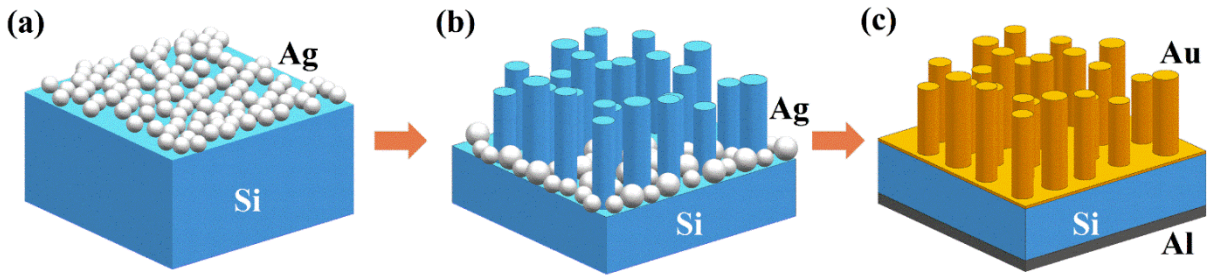

Figure S2. Fabrication process of plasmonic Au/Si nanowires (NWs) using the conventional metal-assisted chemical etching (MACE) method, which involves the deposition of small Ag particles (a), followed by etching of only Si underneath these particles to obtain Si NWs (b). By depositing an Au film of 10 nm, plasmonic Au/Si NWs can be formed. Finally, Al is deposited to form Ohmic contact with n-Si.

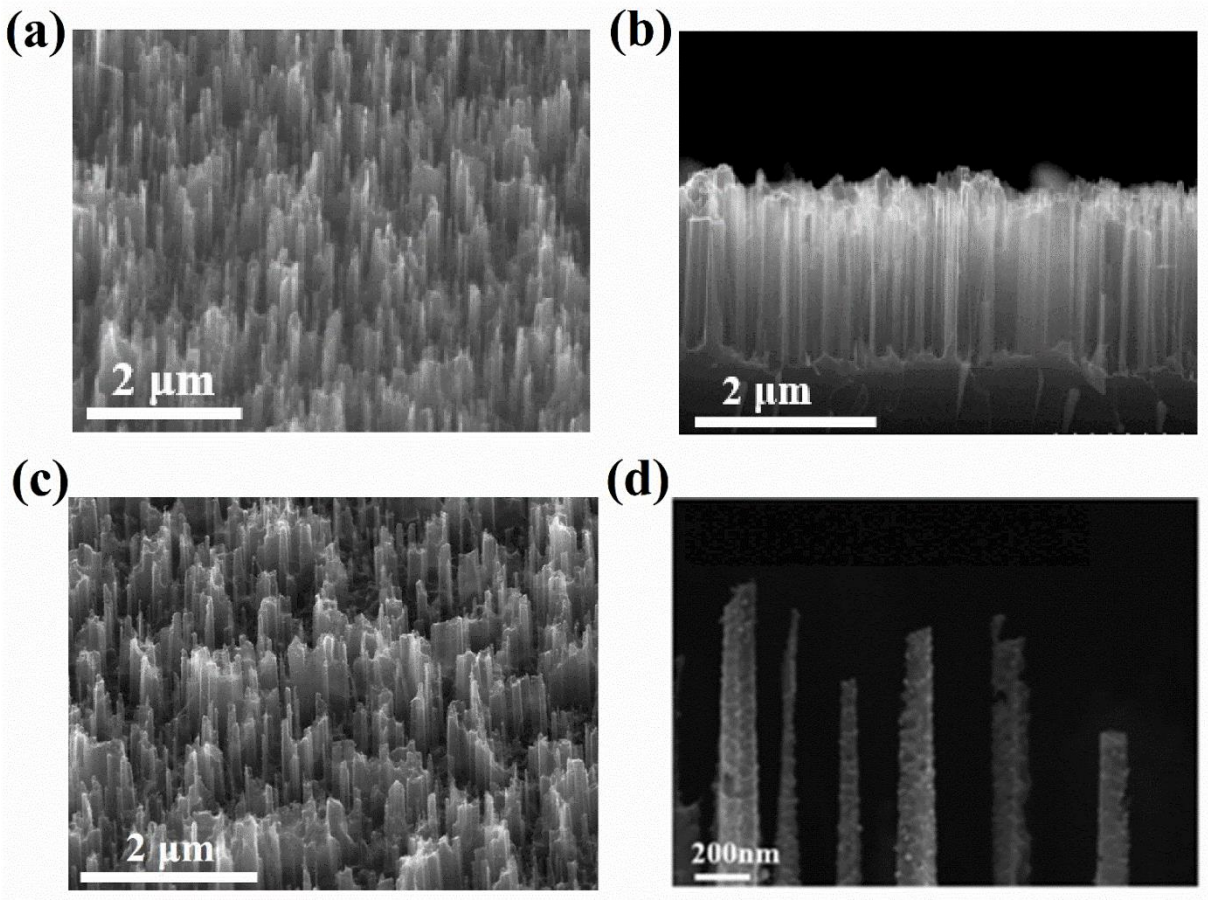

Figure S3. Sectional-view and oblique-view SEM images of Si NWs (a, b) and plasmonic Au/Si NWs.

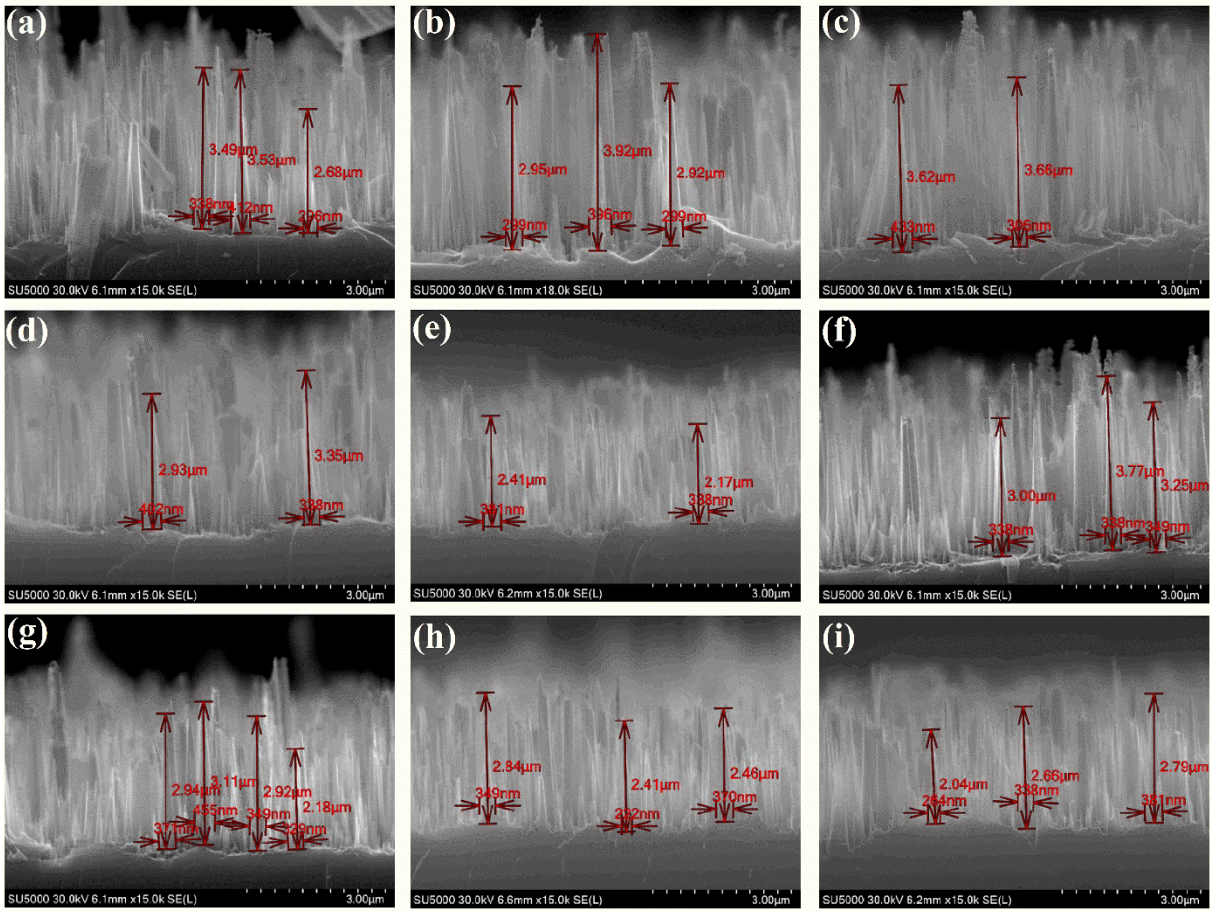

Figure S4. Examples of the measured heights and bottom cross-sectional diameters from 25 Si nanoneedles.

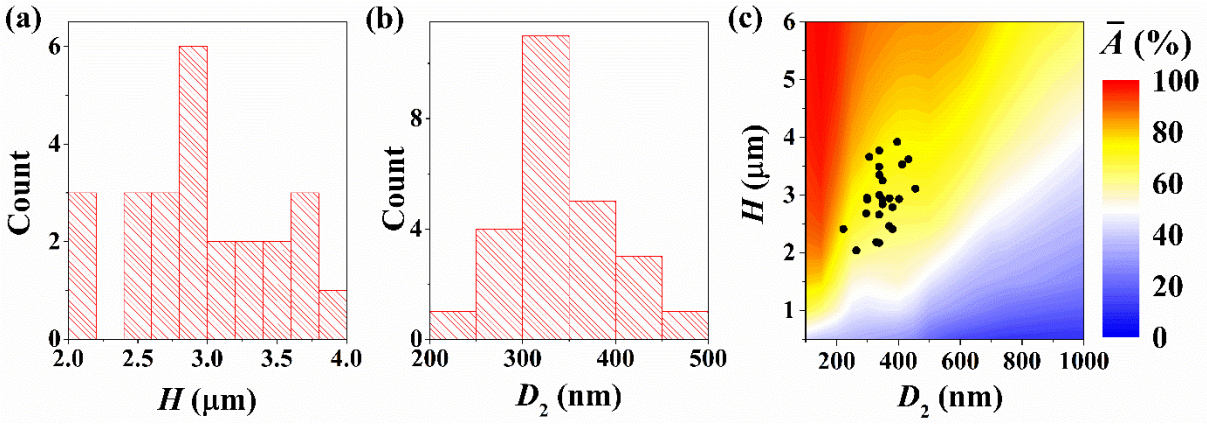

Figure S5. Histogram plot of the height (a) and bottom cross-sectional diameter (b) of the measured nanoneedles. (c) Average absorption of the plasmonic nanoneedles versus the height and bottom cross-sectional diameter, with the corresponding measured values of H and D_2 marked.

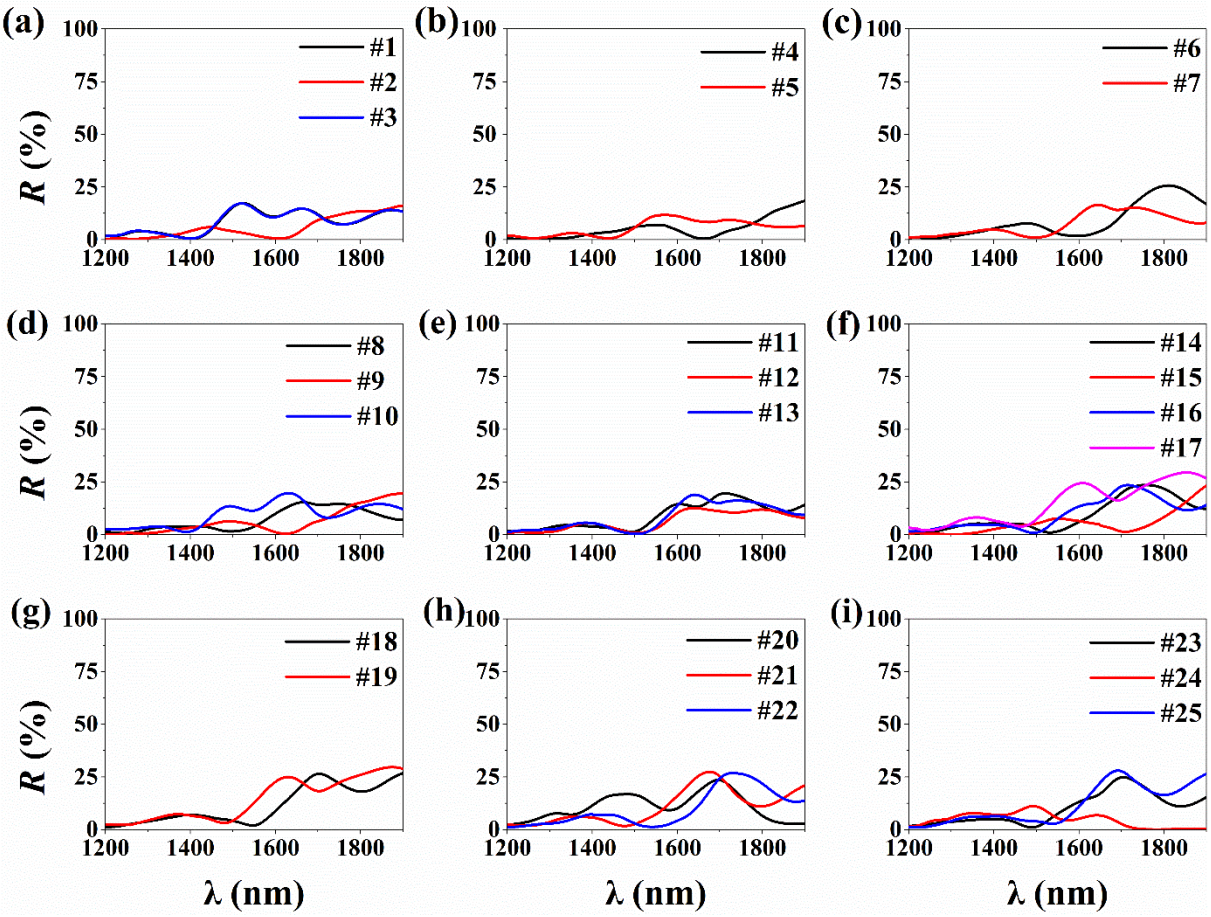

Figure S6. Optical reflection of the plasmonic nanoneedles coated with a 10 nm ultrathin Au film on Si nanoneedles that measured in Figure S4.

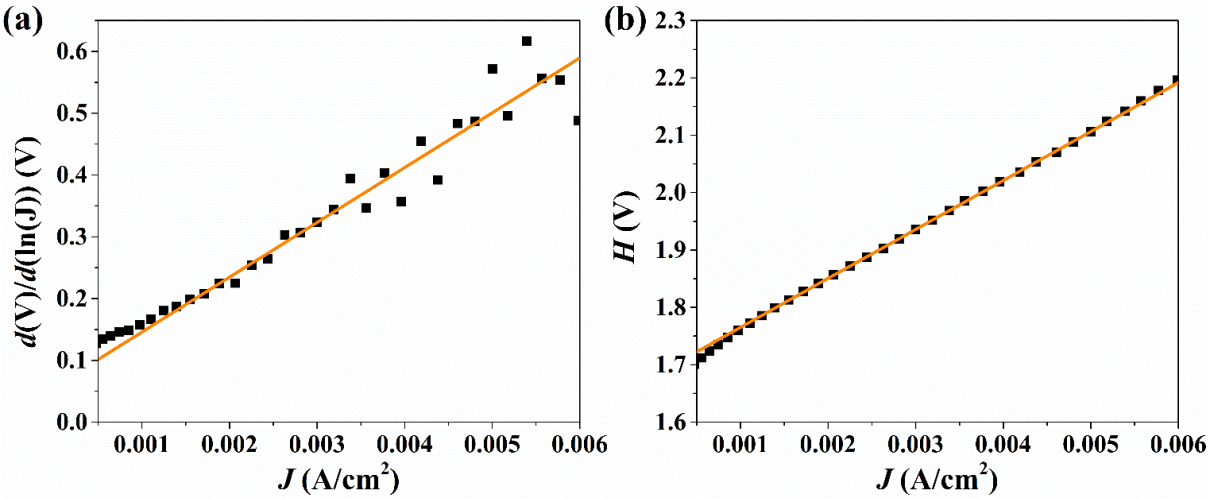

Figure S7. Theoretical fitting to the dark *IV* curves based on thermal emission model to extract barrier height.

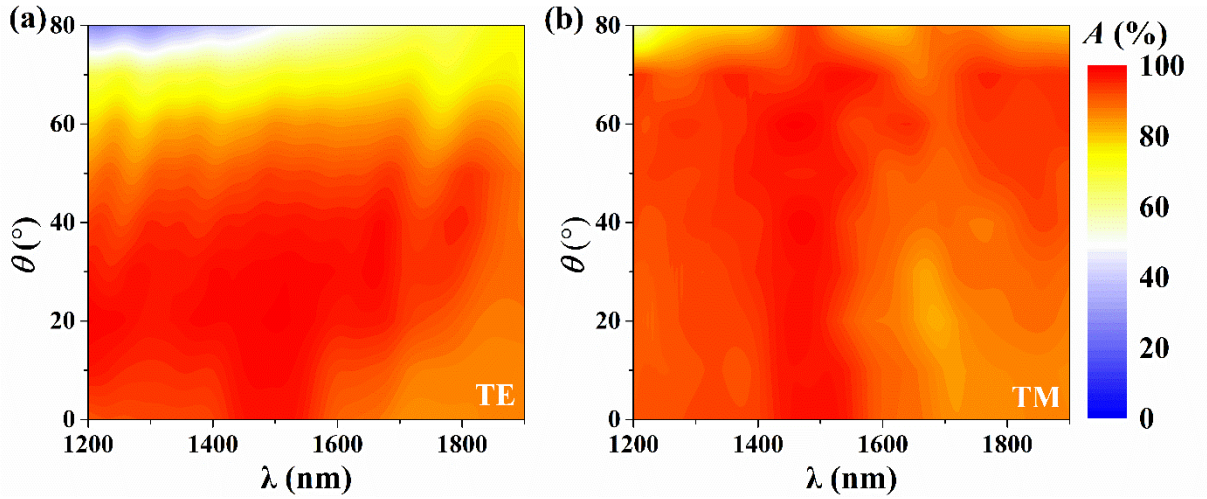

Figure S8. Angular dependent optical absorption in the plasmonic nanoneedles with D_1 = 50 nm, D_2 = 300 nm, and H = 5 μm under (a) TE- and (b) TM-polarized light.